

Physiologically Based Pharmacokinetic Model for Specific and Nonspecific Monoclonal Antibodies and Fragments in Normal Tissues and Human Tumor Xenografts in Nude Mice¹

Laurence T. Baxter, Hui Zhu, Daniel G. Mackensen, and Rakesh K. Jain

Steele Laboratory, Department of Radiation Oncology, Massachusetts General Hospital and Harvard Medical School, Boston, Massachusetts 02114 [L. T. B., H. Z., R. K. J.]; Radiological Sciences Program, Massachusetts Institute of Technology, Cambridge, Massachusetts 02139 [H. Z.]; and Hybritech Incorporated, San Diego, California 92121 [D. G. M.]

ABSTRACT

A physiologically based pharmacokinetic model to describe the biodistribution of a specific monoclonal antibody IgG1 (ZCE025) and its fragments (F(ab')₂ and Fab) and of a nonspecific IgG1 (MOPC21) in normal tissues and a human colon carcinoma xenograft (T380) in nude mice is developed. The model simulates the experimental data on the concentration of these four macromolecules in plasma, urine, heart, lung, liver, kidney, spleen, bone, muscle, skin, GI tract, and tumor. This is the first such model for macromolecules with specific binding. A two-pore formalism for transcapillary solute exchange is used which avoids the oversimplifications of unidirectional transport or a single effective permeability coefficient. Comparison of the model with our biodistribution data shows that: (a) a physiologically based pharmacokinetic model for specific and nonspecific antibodies is able to explain experimental data using as few adjustable parameters as possible; (b) for antibodies and fragments, the tumor itself has no significant influence on the pharmacokinetics in normal tissues; and (c) the two-pore formalism for transcapillary exchange describes the data better than a single-pore model without introducing extra adjustable parameters. Sensitivity analysis shows that the lymph flow rate and transvascular fluid recirculation rate are important parameters for the uptake of antibodies, while for the retention of specific antibodies, extravascular binding is the key parameter. A single-pore model could also obtain a good fit between model and data by adjusting two parameters; however, the estimated permeability was 1000 times higher than with the two-pore model, and the binding affinity was such that approximately five times more material was bound than free in the extravascular space for nonspecific antibody. Setting the binding affinity to zero or reducing the value of the permeability-surface area product did not allow a good fit, even when the lymph flow rate was varied. The present model may be useful in scaling up antibody pharmacokinetics from mouse to man.

INTRODUCTION

Monoclonal antibodies have offered a promising approach to the detection and treatment of solid tumors due to their specific binding with tumor-associated antigens. However, the clinical potential of monoclonal antibodies has not yet been fully realized. There are many physiological, kinetic, and immunological parameters which could adversely affect their uptake, distribution, and catabolism (1, 2). A comprehensive, physiologically based, organ-specific pharmacokinetic model may help in: (a) understanding the factors involved in antibody biodistribution; (b) identifying the key parameters which limit or enhance antibody delivery; (c) designing experiments to obtain these parameters; and, (d) improving diagnosis and therapy. Such models have been developed for low molecular weight drugs (for review, see Refs. 3 and 4). Although there are several compartmental

models for antibody pharmacokinetics (for review, see Ref. 5), they are not physiologically based, and hence not easily amenable to scale-up to patients. Covell *et al.* (6) have developed a physiologically based pharmacokinetic model for an i.v. injected nonspecific, murine, homologous whole IgG1 (MOPC21) and its F(ab')₂ and Fab fragments in tumor-free mice. Although useful, their model has two limitations; it does not include a tumor compartment, and it is not readily applicable for specific antibodies. Our previous pharmacokinetic models for antibody transport focused only on the tumor and did not consider normal organs (7, 8).

We present here a physiologically based model to describe the pharmacokinetics of a specific monoclonal antibody and its F(ab')₂ and Fab fragments in nude mice bearing human tumor xenografts. Two novel features characterize our approach: (a) the antibody and its fragments have nonspecific, nonsaturable binding in both normal and tumor tissues and specific, saturable binding in the tumor tissue; and, (b) a two-pore formalism (9) is used to describe transcapillary exchange. Specific, reversible, saturable binding is assumed to occur in the tumor, and elevated, reversible, nonsaturable binding is assumed to occur in the bone marrow. This physiologically based pharmacokinetic model may be used: (a) to define quantitatively the pharmacokinetic differences between whole IgG and its fragments; (b) to examine how these pharmacokinetic differences may be used to improve detection and treatment of tumors; (c) to study the effects of physiological and physicochemical parameters on the pharmacokinetic differences between antibodies with both nonspecific and specific binding *versus* antibodies with only nonspecific binding; and (d) to provide a baseline model for possible scale-up to humans.

MATERIALS AND METHODS

Experimental Protocol. The biodistribution of i.v. administered ¹¹¹In-labeled specific monoclonal antibody ZCE025 IgG, its fragments F(ab')₂ and Fab, and nonspecific monoclonal antibody MOPC21 was measured in 22-g female *nu/nu* mice (22.15 ± 1.6 g body weight) bearing T380 human colon carcinoma xenografts. The tumor was grown s.c. for 7-14 days until it reached the size of a few hundred milligrams (472 ± 110 mg). The T380 line is known to produce and secrete CEA² (10). ZCE025 (11), also known as monoclonal antibody 35, is a murine IgG1 monoclonal antibody which reacts with human CEA. MOPC21 has no known antigen and was used as an irrelevant control. The Fab and F(ab')₂ fragments of ZCE025 were prepared by enzymatic digestion and purified by size exclusion chromatography. The diethylenetriaminepentaacetic acid-conjugated antibodies and fragments were labeled with ¹¹¹In with an incorporation greater than 90% as determined by thin layer chromatography. The dose administered was 10 μCi (3.8 μg MOPC21-IgG, 10.9 μg ZCE025-IgG, 4.0 μg ZCE-F(ab')₂, and 8.0 μg ZCE-Fab) injected into the tail vein. The biodistributions were determined in six mice each at 4, 24, 48, 72, 96, and 120 h after injection using a gamma well counter (Tracor Analytic, Elk Grove Village, IL) with the procedure described in (10). The percentage of injected dose per gram in an organ or tissue was measured in the blood, heart, lung, liver, kidney, muscle, skin, spleen, GI tract, bone (including marrow), and

Received 5/21/93; accepted 1/14/94.

The costs of publication of this article were defrayed in part by the payment of page charges. This article must therefore be hereby marked *advertisement* in accordance with 18 U.S.C. Section 1734 solely to indicate this fact.

¹ This work was supported by a grant from Hybritech and National Cancer Institute Grant CA-49792. This work was presented at the 10th International Hammersmith Conference on Advances in the Applications of Monoclonal Antibodies in Clinical Oncology, Paphos, Cyprus, May 3-5, 1993, and the 85th Annual Meeting of the American Institute of Chemical Engineers, St. Louis, MO, November 7-12, 1993.

² The abbreviations used are: CEA, carcinoembryonic antigen; GI, gastrointestinal. Also see Appendix A.

tumor. After removal from the animal, tissues were weighed, and radioactivity measured in a gamma counter as

$$\text{Percentage of injected dose/g} = \frac{\text{Tissue cpm}}{\text{Injected cpm}} \times \frac{100}{\text{Weight of tissue}}$$

where cpm are adjusted for background and decay. The relative cardiac output was also determined for these organs using the RbCl uptake method (12). The binding affinity of the antibodies against CEA was determined via Scatchard analysis (13, 14). The stability of the ^{111}In -antibody linkage was verified in two ways. *In vitro* testing of the radioisotope stability at 37°C in serum indicated no more than 0.22% loss of label per day over a 5-day period. The *in vivo* stability was checked by studying the radioactivity 24 and 120 h following a 10- μCi tail vein injection of ZCE025-IgG (10). At these time points, essentially all of the radioactivity recovered from the blood was associated with cells or protein as determined by ultrafiltration (Centrifree; Amicon, Beverly, MA). Greater than 50% of the radioactivity in the urine at 24 and 120 h was associated with protein. There was 5 to 26% and 14 to 26% of the injected dose recovered in the urine at 24 and 120 h postinjection, respectively. The total recovered activity was always estimated from the sum of the tissue samples and was generally greater than 80% of the injected amount.

Model Development. A physiologically based model was developed to describe the pharmacokinetics of ZCE025, its fragments, and MOPC21 in T380-bearing nude mice. The physiologically based pharmacokinetic approach uses measurable physiological parameters, such as organ volumes, blood flow rates, and permeability coefficients, and hence may permit *a priori* prediction of drug biodistribution and scale-up between species (15, 16). The organs and tissues included in our model are plasma, bone including bone marrow, heart, lung, liver, kidney, spleen, GI tract, skin, muscle, and the T380 tumor xenograft. They account for approximately 90% of the injected radiolabeled nuclides in the mice immediately after injection.

Our model includes all the key processes related to: (a) blood circulation through these vital organs and tissues; (b) exchange across the capillary wall in these organs and tissues; (c) return of antibody (or its fragments) from the interstitial space to the bloodstream via lymph; (d) reversible and nonsaturable nonspecific binding of antibody (or its fragments) in the extravascular compartment; (e) reversible and saturable specific binding in the tumor tissue and bone marrow; (f) a catabolic clearance process in all these organs and tissues; and (g) elimination through urine.

We further divide each organ or tissue into two subcompartments, vascular space and extravascular space, which includes interstitial space and cellular space. We assume that the transcapillary exchange of antibodies and fragments between vascular (plasma) and interstitial space occurs via both passive diffusion and convection and that there is no antibody accumulation in the cellular space. To quantitatively describe the transcapillary exchange in each organ, a two-pore model proposed by Rippe and Haraldsson (9) was used. In this filtration model, both fluid and solute exit the blood vessel through large pores (~250-Å diameter), while primarily fluid and very small molecules pass through small pores (~45-Å diameter). Even under isogravimetric (no net flow) conditions, there is a recirculation of fluid which leads to enhanced macromolecular extravasation. This may be especially important in tumors, where large regions may exist without net fluid filtration due to elevated interstitial pressure (17–19). In the extravascular space, the antibody can bind nonspecifically or specifically with tumor-associated antigens. The model also accounts for degradation and elimination of antibodies (See Appendix B for details).

Model Parameters. Rather than using nonphysiological parameters or adjusting all parameters, it is advantageous to fit the data with parameters that have well-defined physiological or physical meaning and are experimentally measurable. Many parameter values used in the model are from the literature. In cases where no *in vivo* data was available or there was large uncertainty associated with reported values, we have estimated the parameters by curve fitting (see "Parameter Estimation Procedure"). We have made a concerted effort to have as few adjustable parameters as possible in the model simulations.

The physiological parameters used in this model include excretion rate through urine and tumor-associated antigen concentration, and for each organ, plasma flow rate, transcapillary fluid filtration rate, net lymph flow rate, vascular, interstitial, and total volume, and catabolic clearance rate. In principle, all these parameters have direct and well-defined physiological meaning

and could be measured experimentally. Organ volumes and plasma flow rates were obtained from the literature (except for tumor, bone, and skin blood flow rates, which we determined experimentally). In many tissues, the vascular space occupies approximately 10% or less of total organ volume, while the interstitial space occupies about 10–34% of the total organ values (20, 21). A typical value for tumors is approximately 7% vascular space and 38% interstitial space (which is much greater than that in normal tissues). The estimated values used for different organs and tissues were based upon literature values (Refs. 20–22; Tables 1 and 2). The permeability-surface area product was obtained by scaling the value for albumin (9) by the diffusion coefficient in normal tissue (similar to Refs. 23–25). This *PS* product was taken to be 10-fold higher for tumor and liver due to their known elevated permeabilities (25–27). The binding affinity for specific IgG was taken to be zero in all organs except the tumor, with nonspecific (and nonsaturable) binding occurring in the bone marrow. In the absence of experimental data, the rate constants for catabolism in the tissues were set to zero. These fixed, physiological parameters are summarized in Table 1 (while adjustable parameters are given in Table 2).

For each species, there are permeability and osmotic reflection coefficients (for both large and small pores), binding kinetic rate constants (association and dissociation), and a partition coefficient. In the absence of data for partition coefficients, a value of unity was chosen for each species. In this model, a reversible, nonsaturable, first order binding process was assumed for nonspecific binding in all organs (e.g., bone marrow), while a reversible, saturable binding process was assumed for specific binding with tumor-associated antigen in the tumor tissue. Table 3 gives the parameters which differ from one molecular species to another but were kept fixed throughout the simulations. The binding affinities for specific IgG were taken to be zero in all organs except the tumor and bone, where they were treated as adjustable parameters. We chose literature values for the maximum antigen concentration in the tumor, $1.18 \times 10^{-8} \text{ M}$ for IgG and $F(\text{ab}')_2$ and $2.35 \times 10^{-8} \text{ M}$ for the Fab fragment (28). T380 colon carcinoma is known to secrete CEA into the plasma; however, the concentration is much lower than found in the tumor, typically by a factor of 100–1000 (29). Hence, the antigen was assumed to be found nowhere outside the tumor for the present simulations. The effect of shed antigen could easily be included in our model if such data were available.

Parameter Estimation Procedure. In cases when the parameter values were not available, they were estimated by a standard weighted least squares fit of the model to the data (with a weight of $1/y_i$, where y_i is the model solution at time point i , to account for the approximately log-normal distribution). An iterative estimation procedure was used as follows. The plasma data was fit using a triexponential function (8)

$$C_p/C_p^0 = \alpha_1 \exp(-\lambda_1 t) + \alpha_2 \exp(-\lambda_2 t) + (1 - \alpha_1 - \alpha_2) \exp(-\lambda_3 t)$$

Table 1 Plasma flow rates and organ volumes

Organ	Plasma (ml/min)	Total volume (ml) ^a	Vascular volume (ml)	Interstitial volume (ml)
Plasma	4.38 ^b	0.774	0.774 ^a	0.000 ^c
Bone	0.17 ^b	1.500	0.080 ^d	0.280 ^e
Heart	0.28 ^b	0.133	0.007 ^d	0.019 ^e
Kidney	0.80 ^b	0.298	0.030 ^d	0.101 ^c
Liver	1.10 ^b	0.951	0.095 ^d	0.190 ^c
Lung	4.38 ^b	0.191	0.019 ^d	0.057 ^c
Muscle	0.80 ^f	7.924	0.150 ^d	1.032 ^c
Skin	1.21 ^f	2.940	0.200 ^d	0.999 ^c
Spleen	0.05 ^b	0.100	0.010 ^d	0.020 ^c
GI tract	0.90 ^b	3.450	0.100 ^d	0.600 ^e
Tumor	0.10 ^f	0.472	0.033 ^c	0.258 ^c

^a Determined by averaging the experimental weight data for each organ and assuming a density of 1 g/ml except for bone, 1.5 g/ml. For blood, 55% of volume is assumed to be plasma.

^b From Ref. 4.

^c From Ref. 20.

^d For well-perfused organs, e.g., kidney, lung, liver and spleen, 10% vascular space is assumed (21). For others, the vascular space ranges from 2 to 8% of the total volume, and the estimation is based on the experimental data of the plasma and organ at early time points.

^e Estimated on the basis of values for similar tissues.

^f Measured experimentally by Rb uptake method.

Table 2 Parameters fitted for each organ^a

Organ	J_{iso} ml/min (ml/min/g)	L_{organ} ml/min (ml/min/g)	k^f (min ⁻¹) of ZCE025			PS_S (Fab) ml/min/g
			IgG	F(ab') ₂	Fab	
Bone	1.4×10^{-5}	6.0×10^{-5} (2.7×10^{-5})	2.5×10^{-3}	5.5×10^{-4}	3.5×10^{-3}	1.0×10^{-3}
Heart	5.6×10^{-5}	1.0×10^{-5} (7.5×10^{-5})	0.0	3.3×10^{-4}	7.0×10^{-4}	1.0×10^{-4}
Kidney	5.6×10^{-4}	1.7×10^{-4} (5.7×10^{-4})	0.0	1.2×10^{-3}	4.0×10^{-2}	5.5×10^{-3}
Liver	4.6×10^{-4}	2.0×10^{-4} (2.1×10^{-4})	0.0	3.6×10^{-4}	3.3×10^{-3}	1.2×10^{-4}
Lung	3.0×10^{-4}	1.0×10^{-4} (5.2×10^{-4})	0.0	3.0×10^{-5}	2.0×10^{-4}	1.3×10^{-4}
Muscle	5.0×10^{-6}	6.0×10^{-4} (7.6×10^{-5})	0.0	2.4×10^{-4}	5.0×10^{-4}	3.0×10^{-4}
Skin	3.0×10^{-5}	1.0×10^{-5} (3.4×10^{-5})	0.0	7.5×10^{-2}	8.5×10^{-4}	4.7×10^{-4}
Spleen	3.0×10^{-5}	2.0×10^{-6} (2.0×10^{-5})	0.0	6.5×10^{-2}	6.5×10^{-3}	8.5×10^{-4}
GI tract	1.0×10^{-6}	7.0×10^{-4} (2.0×10^{-4})	0.0	7.5×10^{-4}	8.5×10^{-4}	9.3×10^{-4}
Tumor	1.0×10^{-5}	7.0×10^{-5} (1.4×10^{-4})	0.80 ^b	0.16 ^a	0.01 ^a	4.5×10^{-4}

^a MOPC fit J_{iso} and L_{organ} ; ZCE-IgG fit only k^f_{bone} and k^f_{tumor} ; ZCE-F(ab')₂ fit k^f ; and ZCE-Fab fit k^f and PS_S . All other parameters were kept constant. Lymph flow rates are given on both a per organ and per g basis (the latter in parentheses).

^b Specific binding forward rate constant for tumor, $k^{f,sp}$ min⁻¹ ml/pmol; nonspecific k^f taken as zero, with $k^{f,sp} = 0.0085$ min⁻¹, and B_{max} for tumor taken as 1.18×10^{-8} M for IgG and F(ab')₂, and 2.35×10^{-8} M for the Fab fragment (28).

Table 3 Molecular species-dependent parameters

Species	R^a	Fixed				Fit	
		B_{max}^b M	σ_L^c	σ_S^b	PS_L^d (ml/min/g)	PS_S^d (ml/min/g)	Urine excretion rate (min ⁻¹)
MOPC IgG	1.0	0.00	0.26	0.98	2.66×10^{-6}	7.80×10^{-6}	0.00033
ZCE IgG	1.0	1.18×10^{-8}	0.26	0.98	2.66×10^{-6}	7.80×10^{-6}	0.00026
ZCE F(ab') ₂	1.0	1.18×10^{-8}	0.11	0.96	7.98×10^{-6}	2.34×10^{-5}	0.0011
ZCE Fab	1.0	2.35×10^{-8}	0.10	0.95	2.42×10^{-5}	see Table 2	0.0077

^a Taken as unity for all species.

^b Antigen concentration from Ref. 28.

^c From Ref. 9.

^d Based on albumin data (9), scaled by diffusion coefficient in normal tissue. Values for tumor and liver are assumed to be 10-fold higher than in other organs.

The data for each organ was fit individually using this smoothed plasma data. To close the loop on the mass balance, the simulations were repeated using the pharmacokinetic model values for the plasma instead of the triexponential fit. The urine clearance rate and other unknown parameters were then varied to obtain the minimal weighted least squares fit of the model to the plasma data. The procedure was repeated (fitting each organ individually with the same plasma forcing function, followed by calculating the new plasma concentrations from the model) until the parameter values converged within 1%.

The estimation of parameters for different molecular species was carried out sequentially (Table 4): (a) the nonspecific IgG data for each organ was fit using two adjustable parameters, the transcapillary fluid flow rate (filtration rate of fluid through large pores) and the lymph flow rate (the *net* filtration rate, collected by lymphatic vessels and returned to the bloodstream). The values obtained from this fit were then maintained constant for the remaining three molecular species; (b) the specific IgG data was fit keeping all parameters the same as for the MOPC21 except for adjusting the binding affinity in tumor and bone. All other organs had no adjustable parameters. For the F(ab')₂ fragment, the binding affinity in each organ was treated as an adjustable parameter; and (c) for the Fab fragment, it was necessary to use two adjustable parameters, the binding affinity (which determines the fraction that is bound or internalized by cells) and the small pore permeability coefficient [which appears to be much more important for this small fragment than for whole IgG or F(ab')₂].

RESULTS

Comparison of Model with Data. The values of the plasma flow rates were available from the literature for all organs except tumor, bone, and skin. Therefore, values for these three organs were determined experimentally (Table 1). The percentage cardiac output to

various organs and tissues for 22-g nude mice was determined experimentally by ⁸⁶Rb uptake method (12). The plasma flow rates to each organ were then determined based on the published average cardiac output of 22-g nude mice (4). The flow rates measured for the remaining organs were similar to literature values (data not shown).

Fig. 1 shows the model simulations for MOPC21 for the plasma, tumor, and nine normal tissues: liver; kidney; lung; heart; skin; muscle; spleen; GI tract; and bone. For each organ, there were two adjustable parameters, lymph flow rate and isogravimetric recirculation rate. The ZCE025 results are shown in Fig. 2. The urine clearance rate was 20% lower for the specific antibody. There are no adjustable parameters, except for the binding affinity in the tumor and bone. All parameters were taken from our experiments or the literature (Table 1) or from the MOPC21 simulations (transcapillary fluid flow rates). Fig. 3 and 4 show the model simulations for F(ab')₂ and Fab fragments of ZCE025, respectively. In both cases, the binding affinity was used to fit the data. For the Fab fragment, the permeability of the small pore pathway (PS_s) was also adjusted to obtain the best fit. This sequential method of parameter estimation (Table 4) minimized the number of adjustable parameters for a given simulation.

Sensitivity Analysis. For pharmacokinetic models, it is important not only to know the values of estimated parameters but the effect each unknown or estimated parameter has on the model solution. The relative sensitivity coefficients for the parameters were calculated $[(dC/dP)/(C/P)]$; i.e., the percentage change in the concentration divided by the percentage change in parameter value, P . The maximum value of the sensitivity coefficients and the corresponding times are given in Table 5. Negative values for the sensitivity coefficients mean

Table 4 Parameter estimation procedure

Molecular species	Fixed parameters	Adjustable parameters ^a
MOPC21 IgG	$k_{EL}, k^f, K, Lp, Q, PS_L, PS_S, \sigma_L, \sigma_S, V_v, V_i, V_{tot}$	J_{iso}, L
ZCE025 IgG	$k_{EL}, k^f, K, Lp, Q, PS_L, PS_S, \sigma_L, \sigma_S, V_v, V_i, V_{tot}$ Also J_{iso} and L fixed from MOPC21	k^f for tumor and bone
ZCE025 F(ab') ₂	$k_{EL}, k^f, Lp, Q, PS_L, PS_S, \sigma_L, \sigma_S, V_v, V_i, V_{tot}$ Also J_{iso} and L fixed from MOPC21	k^f
ZCE025 Fab	$k_{EL}, k^f, Lp, Q, PS_L, \sigma_L, \sigma_S, V_v, V_i, V_{tot}$ Also J_{iso} and L fixed from MOPC21	k^f, PS_S

^a Urine clearance rate was also adjusted for each molecular species.

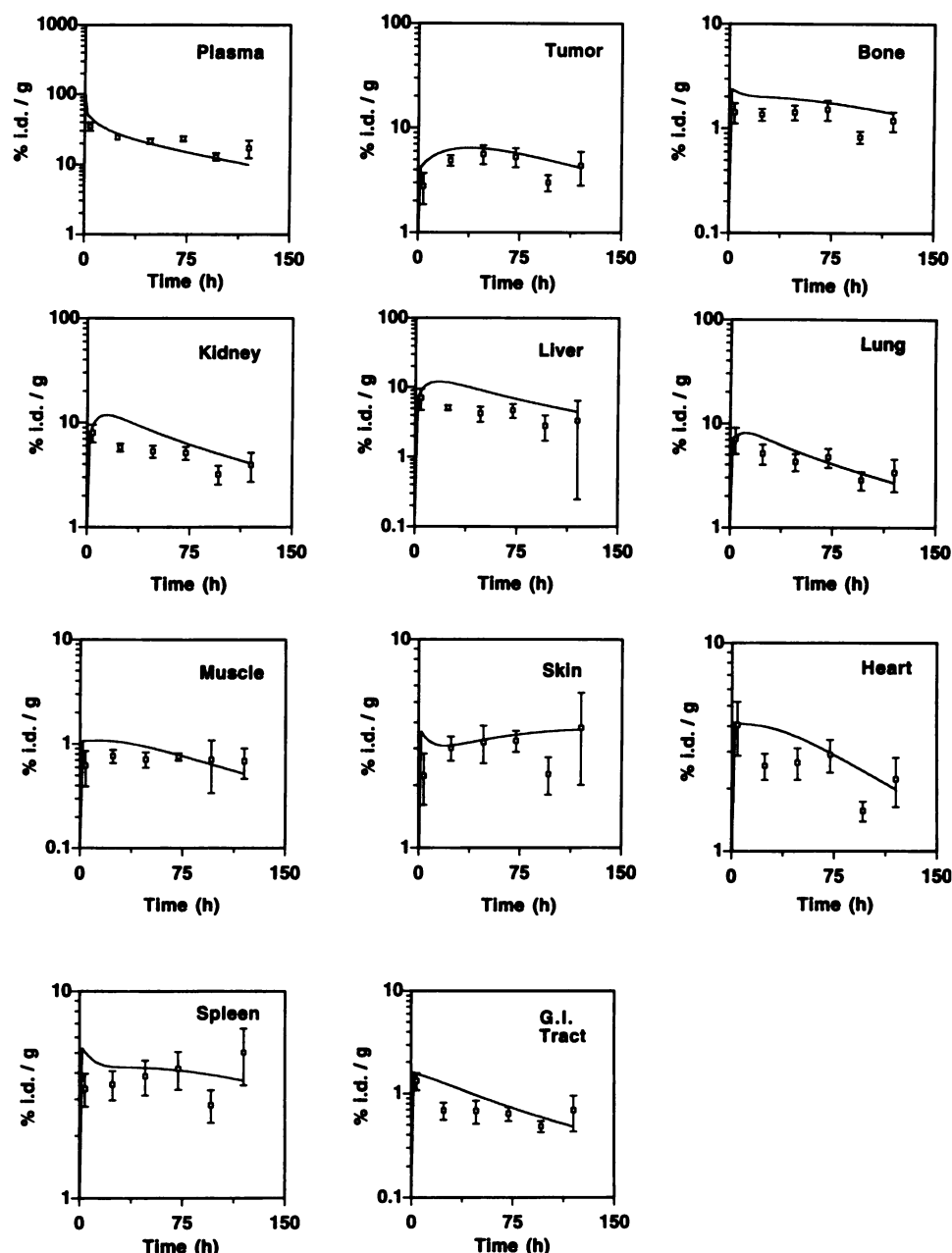


Fig. 1. Experimental data and model simulations for nonspecific IgG1 (MOPC21) (3.8 μ g, i.v.) for plasma, bone, heart, kidney, liver, lung, muscle, skin, spleen, tumor, and GI tract. Note that the Y-axis has different scales for different organs.

that the concentration decreases when the parameter increases; very small absolute values indicate that the concentration is insensitive to that parameter. Note that for nonspecific and specific IgG and its F(ab')₂ fragment, the model solution was insensitive to the plasma flow rate, partition coefficient, osmotic reflection coefficient, and permeability, while the results were sensitive to changes in the plasma, interstitial, and organ volumes; the lymph flow rate; and the fluid recirculation rate under isogravimetric conditions (J_{iso}). For Fab, the model was also sensitive to the vascular permeability of tissues. The effect of the binding coefficient could be quite large, depending on the affinity itself (nonspecific, weak specific, or strong specific binding), with greatest sensitivity in a strongly binding system which is not transport-limited. In such a system, changes in the binding affinity will change the slope of the tissue concentration decay curve, with resultant large changes in tissue concentration at the later time points.

Table 6 shows the relative contribution of convection *versus* diffusion through large and small pores at early time points (when tissue concentrations are near zero) and late time points (when

plasma and free tissue concentrations are similar). For all but the Fab fragment, the dominant mode of transcapillary exchange is convection. Therefore, the model is much more sensitive to changes in the lymph flow rate than to variations in the permeability coefficient for the larger molecules. The permeability coefficient also affected the time required for the interstitial space to come to equilibrium with the plasma.

DISCUSSION

Fig. 1 shows excellent agreement between the model and the MOPC21 data, considering that only the lymph flow rates and transvascular recirculation rates were adjusted. For the ZCE025-IgG data, there is also very good agreement for most organs (Fig. 2), especially since no adjustable parameters were added (except for binding in the tumor and bone marrow). The concentrations in the liver and kidney were nearly constant, unlike those predicted by the model. This suggests there is some binding of this antibody within these organs. The calculated concentration profile

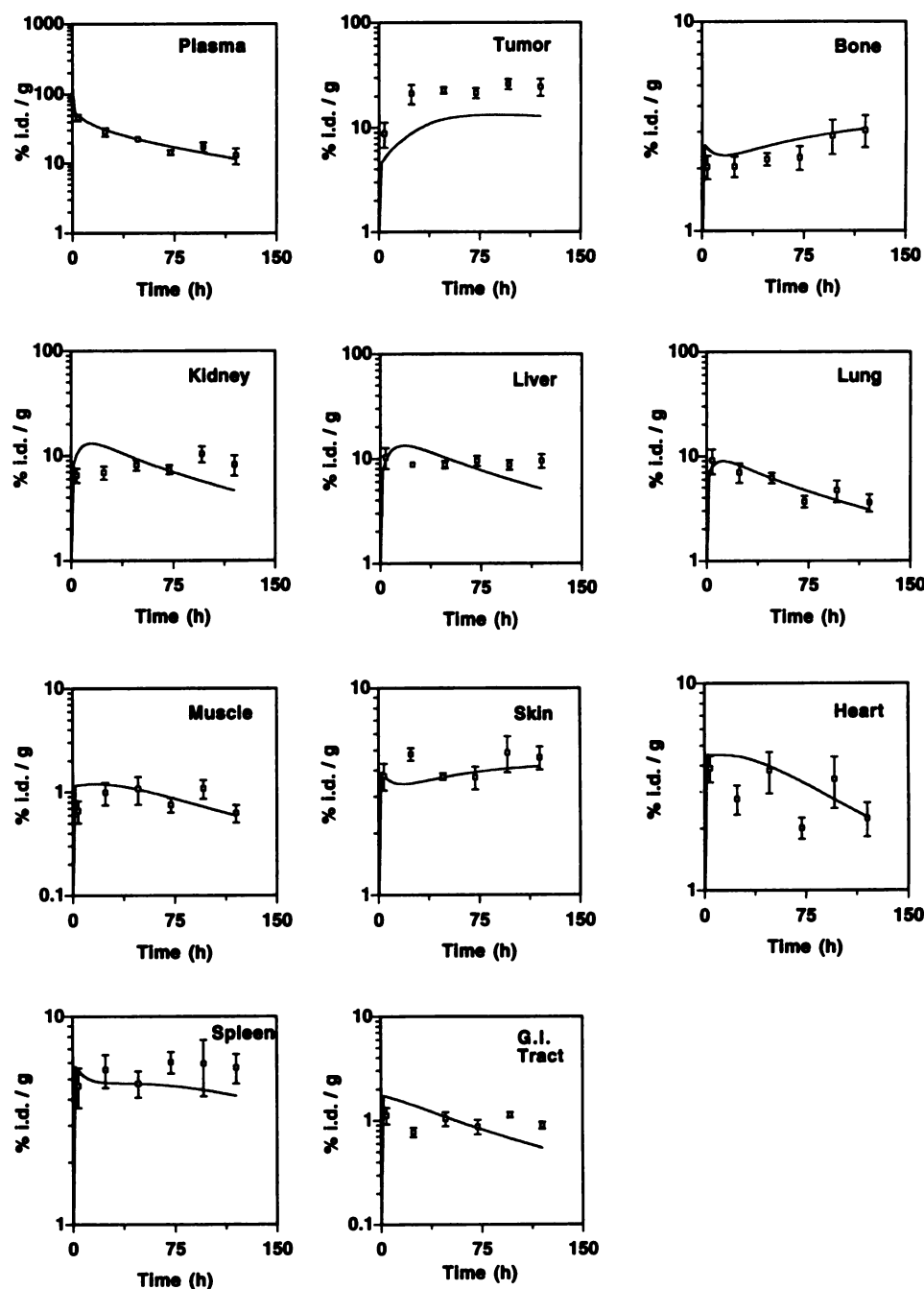


Fig. 2. Experimental data and model simulations for specific IgG1 ZCE025 (10.9 μ g, i.v.) for plasma, bone, heart, kidney, liver, lung, muscle, skin, spleen, tumor, and GI tract. Note that the Y-axis has different scales for different organs.

for the tumor is below the experimental data. This is due to an underestimation of the permeability. The match would be much better for a 25% higher value of PS_s (simulations not shown). The $F(ab')_2$ data was fit by adjusting the amount of nonspecific binding in each organ, allowing excellent agreement between model and data (Fig. 3). While for IgG and $F(ab')_2$ the dominant transvascular pathway is convection, diffusion is more important for the Fab fragment. Therefore, the model was sensitive to PS_s , which had to be adjusted to obtain a good fit for Fab (Fig. 4). The binding rate (k^i) was greater for Fab than for the other species in almost all organs, with greatest binding in the kidney, spleen, liver, and bone. The Fab fragment cleared from the bloodstream so rapidly that there is a large uncertainty in the measured concentration at the latest time point (120 h). Because of this, the measured concentration is lower than that predicted by the model; this is also seen in the kidney, liver, and GI tract.

The quantitative kinetics of nonspecific binding of antibody/fragments in normal tissues is still an important research subject. Currently, there are no *in vivo* experimental data available (30, 31). The baseline values we used are based upon *in vitro* specific binding kinetics. Therefore, the values obtained from the model may provide some useful information. The binding affinity values obtained by best fit of the model to the tumor data were 9.4×10^{-10} , 1.2×10^{-9} , and $1.2 \times 10^{-9} M^{-1}$ for specific-IgG, $F(ab')_2$, and Fab, respectively. These values compare favorably with the *in vitro* measurements of $1.6 \pm 0.9 \times 10^{-10}$, $1.1 \pm 0.4 \times 10^{-9}$, and $1.1 \pm 1.0 \times 10^{-9} M^{-1}$ ($n = 6, 3$, and 3 , respectively). We also note that the values of the model parameters obtained in the simulation for whole ZCE025 are quite close to those for whole MOPC21, as are the pharmacokinetics in all organs except for the tumor. This would be expected in the absence of significant shed antigen in the plasma or antigen expression in normal tissues.

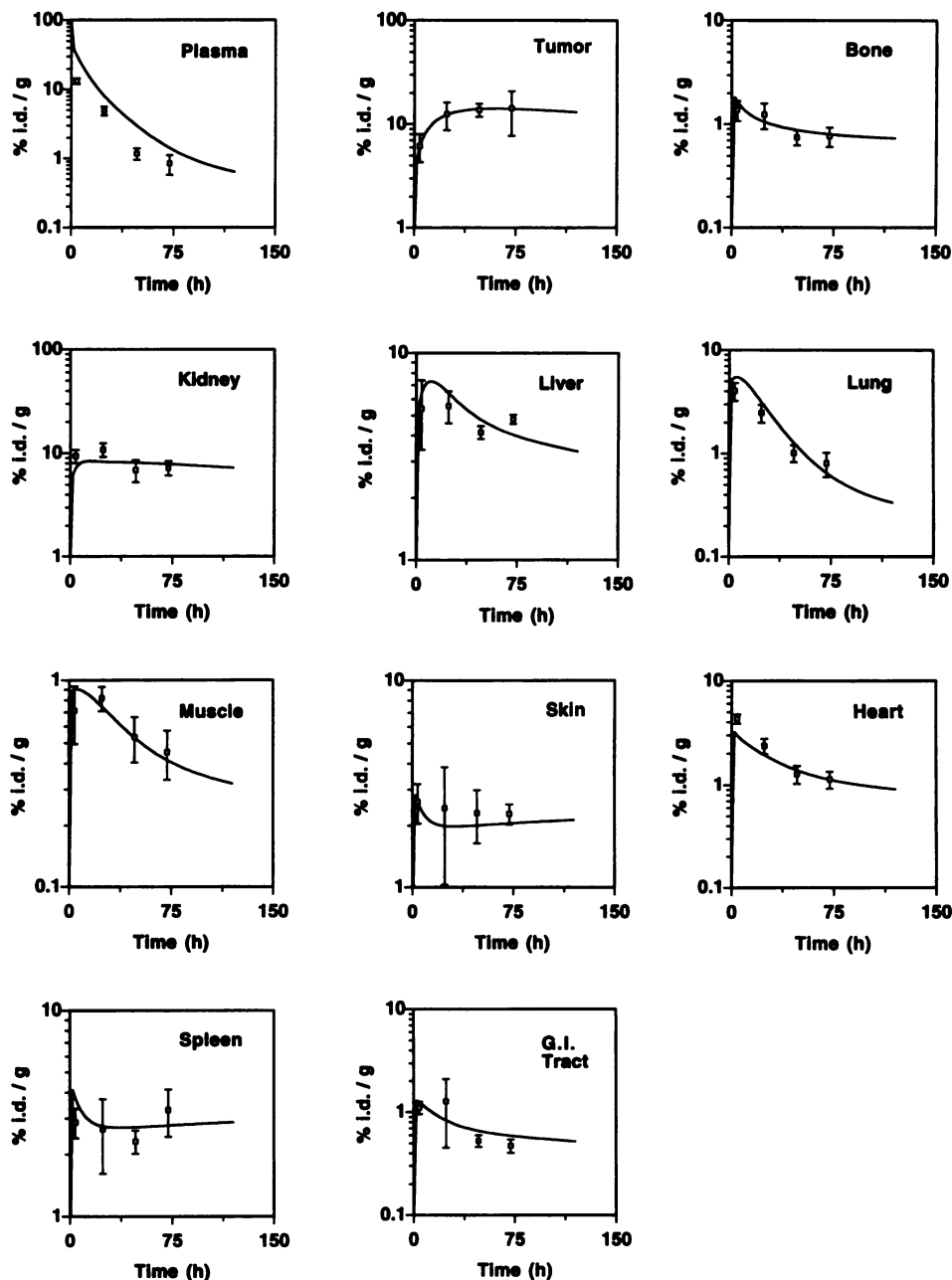


Fig. 3. Experimental data and model simulations of ZCE025 F(ab')₂ (4 µg, i.v.) for plasma, bone, heart, kidney, liver, lung, muscle, skin, spleen, tumor, and GI tract. Note that the Y-axis has different scales for different organs.

While the current simulations have been carried out for ¹¹¹In, other radionuclides may be considered by adjusting the binding and urine clearance parameters to account for altered biodistribution; the mathematical structure of the model will be the same. For example, there is different uptake in the liver for ¹¹¹In- and ¹³¹I-labeled antibodies, while ⁹⁰Y shows increased bone uptake (32).

Comparison of Single-Pore versus Two-Pore Model. Previously in the literature, we and others have used the Patlak equation for the transcapillary solute flux, which is essentially a single-pore model (6–8, 28, 33–38). Some investigators have treated the extravasation of macromolecules as a unidirectional process (39–41). In this case, the solute escapes from the vascular space by convection but may not return. Instead, it is reabsorbed by nearby lymphatics. The lymphatic system is important for the return of fluid and proteins from the tissue spaces back to the bloodstream. Physiologically, all fluid escaping from blood vessels does not become lymph. There may be recirculation of fluid caused by filtration from large pores and absorption via

small pores or from the arterial to venous ends of capillaries. This recirculation of fluid (and hence solute efflux by convection) may occur even under isogravimetric conditions (no net filtration). The two-pore model proposed by Rippe and Haraldsson (9) for transcapillary exchange was used in our model to account for this recirculation. The reason for this is the difference in the osmotic pressure driving forces between large and small pores. Across both the large and small pores, there exist two modes for extravasation of antibodies (active transport and vesicular exchange notwithstanding): diffusion, with a flux proportional to the *PS* product and the concentration difference; and convection, in which the fluid to be absorbed by the lymphatics carries along solute material. For the tumor compartment, although there is no functional lymphatic system, fluid is able to ooze from the tumor periphery, where it may be collected by lymphatic vessels in surrounding normal tissue.

It should be pointed out that J_{iso} is a combination of four parameters: the overall hydraulic conductivity, the fraction of hydraulic

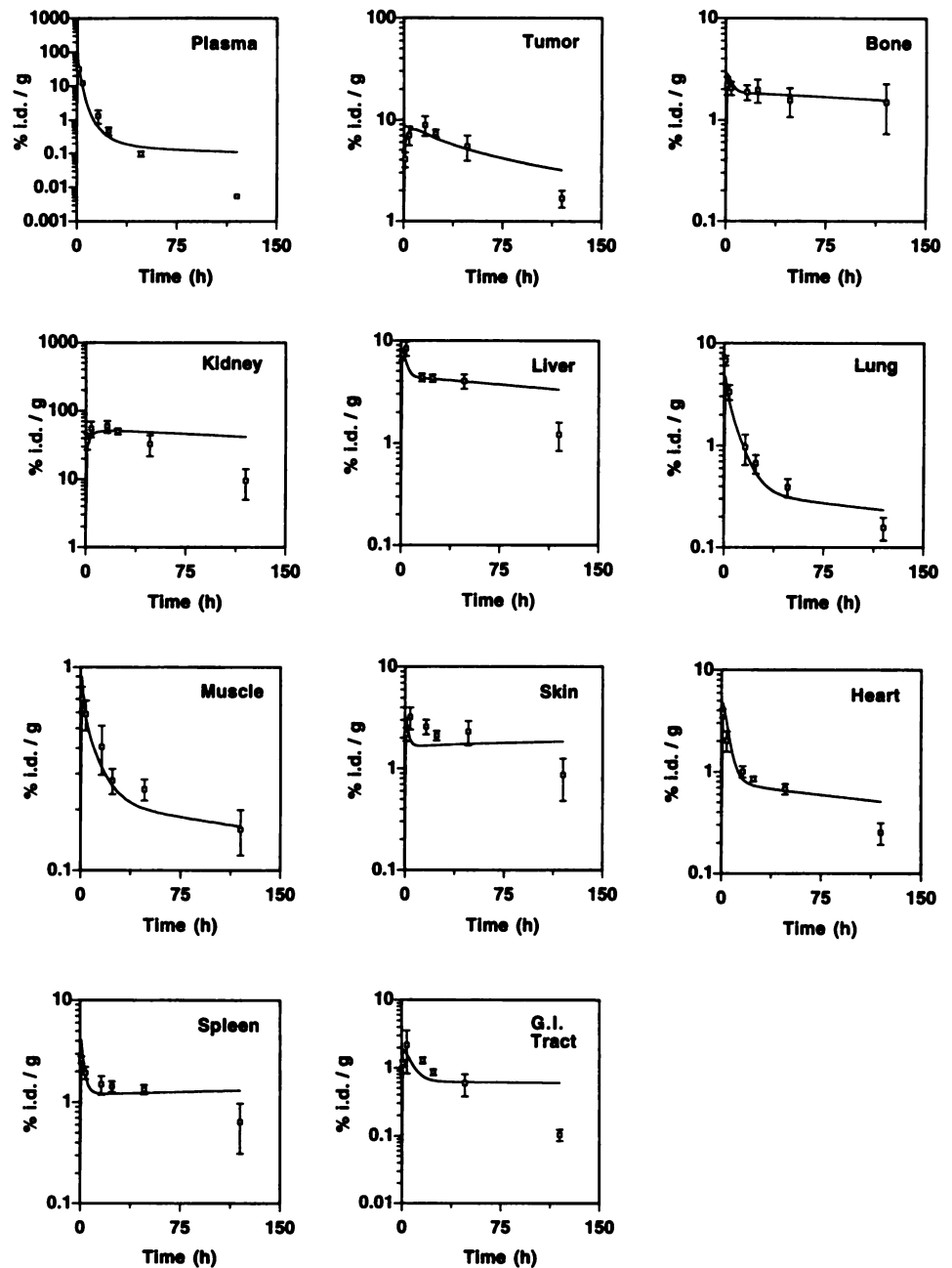


Fig. 4. Experimental data and model simulations of ZCE025 Fab (8 μ g, i.v.) for plasma, bone, heart, kidney, liver, lung, muscle, skin, spleen, tumor, and GI tract. Note that the Y-axis has different scales for different organs.

Table 5 Sensitivity analysis for specific IgG

Parameter	Q	V_{tot}	V_v	V_i	J_{iso}	L	$k^f a$	$k^f b$	R	σ^L	σ_S	PS_L	PS_S	Dose	B_{max}
Max. sens. ^c	0.00	-0.90	1.00	0.91	0.51	-0.68	0.00	16.10	0.01	-0.15	0.18	0.00	0.01	-0.52	14.30
time (h)	120	0	0	120	120	120	120	120	120	120	40	120	6	120	120

^a k^f sensitivity for free:bound ratio of 10:1; max., maximum; sens. sensitivity.

^b k^f sensitivity for bound:free ratio of 10:1.

^c Sensitivity coefficients $(\partial C/\partial P) \cdot [(1/C)/(1/P)]$ for specific IgG in the kidney (except dose and B_{max} in tumor). Values are the same for nonspecific IgG, except coefficients for dose and B_{max} are zero.

conductivity represented by the large pore, the difference in osmotic reflection coefficients, and the transmural osmotic pressure gradient (9). These parameters are difficult to measure and are not currently available except for the estimates of Rippe and Haraldsson (9) for the dog paw. Data for tumors are even more scarce (42). Values of these individual parameters are also dependent on the experimental conditions (e.g., transient versus steady state). In light of these uncertainties, we have chosen to fit J_{iso} for each organ. The value of J_{iso} found by Rippe and Haraldsson (9) was roughly 7×10^{-5} ml/g/min in the

dog paw, which is in agreement with the fit values from our model ranging from 1.0×10^{-5} ml/g/min (skin and heart) to 7.0×10^{-4} ml/g/min (GI tract). The values of the lymph flow rate determined by our model ranged from 0.0008% (skin) to 0.02% (liver and kidney) of the plasma flow rate, which are 10-fold lower than suggested by Rippe and Haraldsson (9). Covell *et al.* (6), on the other hand, chose a much larger value of the lymph flow rate (2 or 4% of the plasma flow rate). Butler *et al.* (43) found that 4.5–10.2% of the plasma flow rate was filtered from the blood vessels and lost through the periphery in a

Table 6 Transvascular exchange pathways

Molecule	Large pore		Small pore	
	Diffusion	Convection	Diffusion	Convection
IgG ^a	0.0% (0.0%) ^b	98.4% (99.9%)	1.7% (0.2%)	0.0% (0.0%)
F(ab') ₂	0.0% (0.0%)	95.8% (102%)	4.3% (-2.3%) ^c	-0.2% (-0.2%)
Fab	0.0% (0.0%)	7.9% (-3.9%)	92% (104.0%)	0.0% (0.0%)

^a Values for IgG hold for both MOPC21 and ZCE025; values for fragments for ZCE025. Values from kidney simulations.

^b Percentages of total solute flux through given pathway at $t = 2$ min (and $t = 120$ h in parentheses).

^c Negative values indicate transport in the direction opposite to the dominant pathway; i.e., for Fab at late time points, most of the material is diffusing back into the interstitium with ~4% going in the other direction due to convection out of the large pore.

tissue-isolated tumor preparation (0.14–0.22 ml/h/g fluid loss rate for 2–5 g tumors). In our model, the lymph flow rate was fit as 0.07% of the plasma flow rate to the tumor (0.0089 ml/h/g). One reason for this difference is that the rate of loss of interstitial fluid is expected to be an order of magnitude greater in tissue-isolated tumors than in tumors surrounded by normal tissue (34). Aukland and Nicolaysen (44) report lymph flow rates ranging from 0.0017–0.072 ml/h/g in various normal tissues. Therefore, the lymph flow rates used in our simulations are physiological but in the lower range of reported values.

As pointed out by Rippe and Haraldsson (9), the use of a single-pore model should overestimate the permeability coefficient. To test this hypothesis with our model, we tried an alternate method for estimating parameters. We used a single-pore model, fixed the lymph flow rate, and fit the data by adjusting the vascular permeability and binding coefficient similar to the method of Covell *et al.* (6). The result for the kidney is shown in Fig. 5. By adjusting two parameters, there was a good fit between model and data. However, note that the estimated PS product is 1000 times higher than with the two-pore model, and the binding affinity (k^f/k^r) is such that approximately five times more material was bound than free in the extravascular space for nonspecific antibody. Setting the binding affinity to zero or reducing the value of PS did not result in a good fit, even if the lymph flow rate was varied. Similar results were seen with the pharmacokinetic model of Covell *et al.* (6) for nonbinding antibody, which required large PS values and large “cellular” volumes (mathematically equivalent to our “bound species”) in order to fit the data. The Peclet number (ratio of transcapillary convection to diffusion) ranged from 0.0015 to 0.1 in the model of Covell *et al.* (6), suggesting primarily diffusive extravasation, while our Peclet number ranged from 0.6 (tumor) to 30 (liver and kidney), which corresponds to convection as the primary mecha-

nism for macromolecular extravasation in all tissues. Using the present pharmacokinetic model with a single-pore required unusually high binding affinities ($k^f/k^r \sim 10$) to achieve a good fit (simulations not shown).

The presence of a two-pore system in the microcirculation may play an important role in the uptake of macromolecules such as antibodies. Boucher and Jain (19) have shown that the microvascular and interstitial pressures in tumors are essentially equal, except in the tumor periphery. The consequence is a nearly zero net fluid filtration rate over central regions of solid tumors. Since convection driven by the transmural pressure difference would be the major pathway, the fluid recirculation may greatly increase the extravasation of macromolecules compared to diffusion alone in central regions of tumors.

Limitations of Current Model. The use of a two-pore formalism for transcapillary exchange, in addition to the sequential approach for parameter estimation, allowed for excellent agreement between the model and the data using a minimum number of adjustable parameters. As mentioned above, the values of some of the parameters used in the model were obtained through fitting the model simulations to the experimental data, such as lymph flow rates, antibody binding kinetics, and catabolic clearance rates. This is mainly because of the paucity of *in vivo* experimental measurements of these physiological parameters. The sensitivity analysis was used to set bounds on the errors resulting from variability or uncertainty in parameters. Insensitivity of the model to a given parameter (e.g., plasma flow rates) leads to small errors in the predicted concentrations but at the same time makes estimation of the parameter difficult. The accuracy of the model would thus be improved by independently obtaining experimental values for those parameters currently obtained by best fit. The current model also does not address issues of antigen shed into the interstitial space and plasma and of spatial heterogeneity within a tumor, for which distributed parameter models (17, 28, 34–39, 45–47) must be developed. Specifically, the importance of transcapillary convection versus diffusion in different regions of the tumor was not addressed here; the model could accommodate this feature through a distributed parameter tumor compartment or a series of lumped tumor compartments. Incorporation of these factors requires data on the kinetics of antigen shedding and detailed spatial concentration profiles. Until such data are available, the current physiologically based pharmacokinetic model should be useful in evaluating the role of physiological processes on antibody delivery and in scaling up bio-distribution patterns to other species including humans (16).

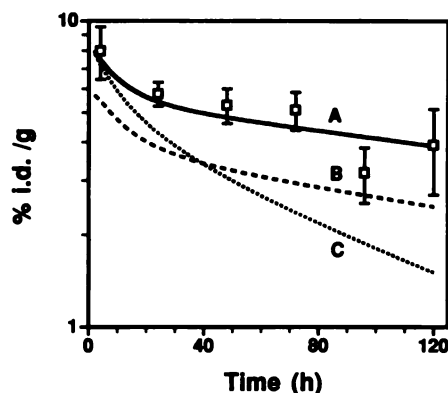


Fig. 5. Comparison of single-pore model with the two-pore model. The calculated concentration profile for nonspecific IgG is shown for the kidney using a single-pore model for transcapillary exchange. Adjusting both PS and k^f/k^r allows for a good fit (A, solid line), but the values of these estimated parameters are unusually high. Keeping PS small (B, dotted line; $PS = 2.32 \times 10^{-6}$ ml/min as in Table 3) did fit the data very well for two adjustable parameters ($L = 2\% Q$ and $k^f/k^r = 10$). Forcing zero binding (C, dashed line) resulted in a worse fit at later time points with the same high values of L and PS as in curve A.

ACKNOWLEDGMENTS

We thank Drs. Paul Kristjansen and Fan Yuan for their helpful comments on this manuscript.

Appendix A: Nomenclature

B_{\max}	Maximum tumor-associated antigen concentration inside tumor tissue (M)
C_{pl}	Antibody concentration in plasma (M)

$C_{v,organ}$	Antibody concentration in the vascular space of each organ (M)
$C_{i,organ}^f$	Free antibody concentration in the interstitium for each organ (M)
$C_{i,organ}^b$	Bound antibody concentration in the interstitium for each organ (M)
C_{TOT}	Average concentration in each organ (M)
$J_{iso,organ}$	Fluid recirculation flow rate for each organ (= flow rate through large pore into the interstitial space for $L = 0$; ml/min)
$J_{S,organ}$, $J_{L,organ}$	Transcapillary fluid flow rate (vascular \rightarrow interstitial) for each organ (ml/min) via small and large pores, respectively
J_{V-1}	Transcapillary solute exchange rate (moles/min)
$k_{EL,organ}$	Catabolic elimination rate for each organ (ml/min)
k^f, k^b	Association and disassociation rate constants for the binding of antibodies or fragments (min^{-1}) ($k^{f,sp}$, $\text{M}^{-1} \text{min}^{-1}$, and $k^{b,sp}$, min^{-1} for specific binding)
L_{organ}	Lymph flow rate of each organ (ml/min)
L_p	Hydraulic conductivity of the vessel wall ($\text{cm mmHg}^{-1} \text{min}^{-1}$)
Q_{organ}	Plasma flow rate to each organ (ml/min)
$Pe_{L,organ}$, $Pe_{S,organ}$	Peclet number, ratio of convection to diffusion across large and small pores ($= J(1 - \sigma)/PS$)
$PS_{L,organ}$, $PS_{S,organ}$	Permeability-surface area product for each organ (min^{-1}) for large and small pores, respectively
U	Excretion rate constant for urine clearance via kidney (ml/min)
$V_{i,organ}$	Interstitial space of each organ (ml)
$V_{v,organ}$	Vascular space of each organ (ml)
$V_{T,organ}$	Total volume of each organ (ml)
σ_L, σ_S	Osmotic reflection coefficient for large and small pores, respectively

Appendix B: Mathematical Model and Governing Equations

The mass balance equations for the pharmacokinetic model describe the circulation of antibodies and fragments throughout the body of a 22-g nude mouse (Fig. B1). Each organ is further divided into two subcompartments, the vascular space and extravascular space, with both free and bound species in the extravascular space (Fig. B2). Inside these organs or tissues, the net flux of antibodies and fragments across the capillary between plasma and interstitial fluid is determined by the following equations according to the two-pore model proposed by Rippe and Haraldsson (9)

$$J_{V-1} = J_{L,organ}(1 - \sigma_L)C_{v,organ} + PS_{L,organ}\left(C_{v,organ} - \frac{C_{i,organ}^f}{R_{organ}}\right)\frac{Pe_L}{e^{Pe_L} - 1} + J_{S,organ}(1 - \sigma_S)C_{v,organ} + PS_{S,organ}\left(C_{v,organ} - \frac{C_{i,organ}^f}{R_{organ}}\right)\frac{Pe_S}{e^{Pe_S} - 1} \quad (\text{B-1})$$

and

$$J_{L,organ} = J_{iso,organ} + \alpha_L L_{organ}; \quad J_{S,organ} = -J_{iso,organ} + \alpha_S L_{organ}$$

with

$$J_{iso,organ} = \alpha_L \alpha_S L_p S(\sigma_S - \sigma_L) \Delta \pi$$

Here $J_{L,organ}$ and $J_{S,organ}$ are the fluid flow rates across the capillary wall in each organ through large and small pores, respectively, and L_{organ} is the lymph flow rate of each organ. $PS_{L,organ}$ and $PS_{S,organ}$ are the product of permeability and the surface area of the organ for large and small pores, respectively. Pe is the corresponding Peclet number, ($= J(1 - \sigma)/PS$), where σ_x is the osmotic reflection coefficient. R_{organ} is the partition coefficient of the antibody or fragment between the vascular and extravascular space. The equations were solved using LSODE, a software package using Gear's method for stiff equations. (48).

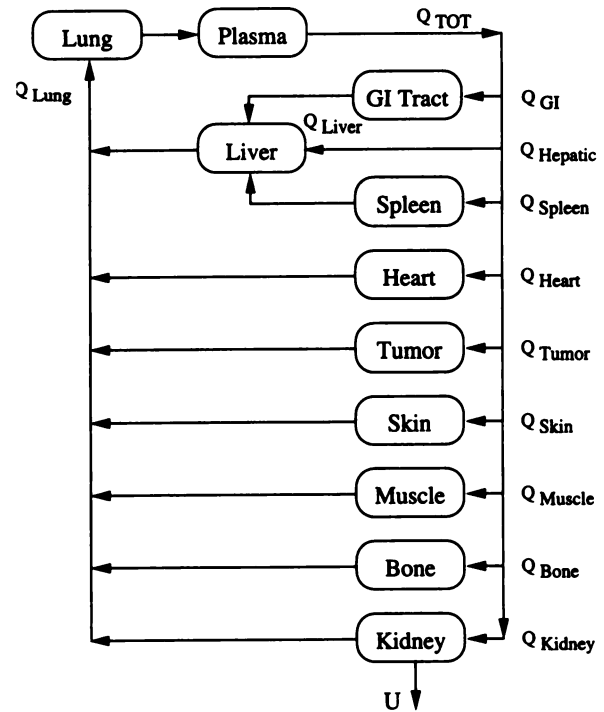


Fig. B1. Schematic of the physiologically based pharmacokinetic model.

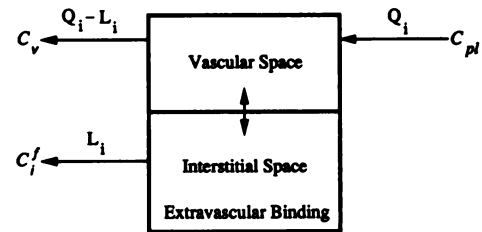


Fig. B2. Schematic of vascular and extravascular subcompartments in each tissue/organ.

B.1 Mass Balance Equation for Plasma

According to the circulation scheme illustrated above (Fig. B-1) and the transcapillary transport equation for antibodies and fragments, the mass balance equation for the plasma compartment is

$$V_{pl} \left(\frac{dC_{pl}}{dt} \right) = (Q_{lung} - L_{lung})C_{v,lung} + L_{lung}C_{i,lung}^f + L_{liver}C_{i,liver}^f + L_{gi}C_{i,gi}^f + L_{spleen}C_{i,spleen}^f + L_{kidney}C_{i,kidney}^f + L_{tumor}C_{i,tumor}^f + L_{skin}C_{i,skin}^f + L_{muscle}C_{i,muscle}^f + L_{bone}C_{i,bone}^f + L_{heart}C_{i,heart}^f - (Q_{liver} + L_{gi} + L_{spleen} + Q_{kidney} + Q_{tumor} + Q_{skin} + Q_{muscle} + Q_{bone} + Q_{heart})C_{pl} \quad (\text{B-2})$$

There is an additional constraint on the volumetric flow rates as

$$Q_{lung} = Q_{liver} - L_{liver} + Q_{kidney} - L_{kidney} + Q_{tumor} - L_{tumor} + Q_{skin} - L_{skin} + Q_{muscle} - L_{muscle} + Q_{bone} - L_{bone} + Q_{heart} - L_{heart} \quad (\text{B-3})$$

B.2 Mass Balance Equations for Lung

Vascular Space

$$\begin{aligned} V_{v,lung} \left(\frac{dC_{v,lung}}{dt} \right) &= (Q_{liver} - L_{liver})C_{v,liver} + (Q_{kidney} - L_{kidney})C_{v,kidney} + (Q_{tumor} - L_{tumor})C_{v,tumor} \\ &+ (Q_{skin} - L_{skin})C_{v,skin} + (Q_{muscle} - L_{muscle})C_{v,muscle} \\ &+ (Q_{bone} - L_{bone})C_{v,bone} + (Q_{heart} - L_{heart})C_{v,heart} - (Q_{lung} - L_{lung})C_{v,lung} \\ &- J_{L,lung}(1 - \sigma_{L,x})C_{v,lung} - PS_{L,lung} \left(C_{v,lung} - \frac{C_{i,lung}^f}{R_{lung}} \right) \frac{Pe_{L,lung}}{e^{Pe_{L,lung}} - 1} \quad (B-4) \\ &- J_{S,lung}(1 - \sigma_{S,x})C_{v,lung} - PS_{S,lung} \left(C_{v,lung} - \frac{C_{i,lung}^f}{R_{lung}} \right) \frac{Pe_{S,lung}}{e^{Pe_{S,lung}} - 1} \end{aligned}$$

Interstitial Space

The free (unbound) concentration of antibody or fragments is given by

$$\begin{aligned} V_{i,lung} \left(\frac{dC_{i,lung}^f}{dt} \right) &= J_{L,lung}(1 - \sigma_{L,x})C_{v,lung} + PS_{L,lung} \left(C_{v,lung} - \frac{C_{i,lung}^f}{R_{lung}} \right) \frac{Pe_{L,lung}}{e^{Pe_{L,lung}} - 1} \quad (B-5) \\ &+ J_{S,lung}(1 - \sigma_{S,x})C_{v,lung} + PS_{S,lung} \left(C_{v,lung} - \frac{C_{i,lung}^f}{R_{lung}} \right) \frac{Pe_{S,lung}}{e^{Pe_{S,lung}} - 1} \\ &- k_{lung}^f C_{i,lung}^f V_{i,lung} + k_{lung}^b C_{i,lung}^b V_{i,lung} - L_{lung} C_{i,lung}^f \end{aligned}$$

The bound concentration of antibody or fragments is given by

$$V_{i,lung} \left(\frac{dC_{i,lung}^b}{dt} \right) = k_{lung}^f C_{i,lung}^f V_{i,lung} - k_{lung}^b C_{i,lung}^b V_{i,lung} - k_{EL,lung} C_{i,lung}^b V_{i,lung} \quad (B-6)$$

B.3 Mass Balance Equations for Liver

Vascular Space

$$\begin{aligned} V_{v,liver} \left(\frac{dC_{v,liver}}{dt} \right) &= (Q_{gi} - L_{gi})C_{v,gi} + (Q_{spleen} - L_{spleen})C_{v,spleen} \quad (B-7) \\ &+ (Q_{liver} - Q_{gi} - Q_{spleen} + L_{gi} + L_{spleen})C_{pl} - (Q_{liver} - L_{liver})C_{v,liver} \\ &- J_{L,liver}(1 - \sigma_{L,x})C_{v,liver} - PS_{L,liver} \left(C_{v,liver} - \frac{C_{i,liver}^f}{R_{liver}} \right) \frac{Pe_{L,liver}}{e^{Pe_{L,liver}} - 1} \\ &- J_{S,liver}(1 - \sigma_{S,x})C_{v,liver} - PS_{S,liver} \left(C_{v,liver} - \frac{C_{i,liver}^f}{R_{liver}} \right) \frac{Pe_{S,liver}}{e^{Pe_{S,liver}} - 1} \end{aligned}$$

Interstitial Space – Free Concentration

$$\begin{aligned} V_{i,liver} \left(\frac{dC_{i,liver}^f}{dt} \right) &= J_{L,liver}(1 - \sigma_{L,x})C_{v,liver} + PS_{L,liver} \left(C_{v,liver} - \frac{C_{i,liver}^f}{R_{liver}} \right) \frac{Pe_{L,liver}}{e^{Pe_{L,liver}} - 1} \quad (B-8) \\ &+ J_{S,liver}(1 - \sigma_{S,x})C_{v,liver} + PS_{S,liver} \left(C_{v,liver} - \frac{C_{i,liver}^f}{R_{liver}} \right) \frac{Pe_{S,liver}}{e^{Pe_{S,liver}} - 1} \\ &- k_{liver}^f C_{i,liver}^f V_{i,liver} + k_{liver}^b C_{i,liver}^b V_{i,liver} - L_{liver} C_{i,liver}^f \end{aligned}$$

Interstitial Space – Bound Concentration

$$V_{i,liver} \left(\frac{dC_{i,liver}^b}{dt} \right) = k_{liver}^f C_{i,liver}^f V_{i,liver} - k_{liver}^b C_{i,liver}^b V_{i,liver} - k_{EL,liver} C_{i,liver}^b V_{i,liver} \quad (B-9)$$

B.4 Mass Balance Equations for Tumor

Vascular Space

$$\begin{aligned} V_{v,tumor} \left(\frac{dC_{v,tumor}}{dt} \right) &= Q_{tumor} C_{pl} - (Q_{tumor} - L_{tumor})C_{v,tumor} \quad (B-10) \\ &- J_{L,tumor}(1 - \sigma_{L,x})C_{v,tumor} - PS_{L,tumor} \left(C_{v,tumor} - \frac{C_{i,tumor}^f}{R_{tumor}} \right) \frac{Pe_{L,tumor}}{e^{Pe_{L,tumor}} - 1} \\ &- J_{S,tumor}(1 - \sigma_{S,x})C_{v,tumor} - PS_{S,tumor} \left(C_{v,tumor} - \frac{C_{i,tumor}^f}{R_{tumor}} \right) \frac{Pe_{S,tumor}}{e^{Pe_{S,tumor}} - 1} \end{aligned}$$

Interstitial Space – Free Concentration

$$\begin{aligned} V_{i,tumor} \left(\frac{dC_{i,tumor}^f}{dt} \right) &= J_{L,tumor}(1 - \sigma_{L,x})C_{v,tumor} + PS_{L,tumor} \left(C_{v,tumor} - \frac{C_{i,tumor}^f}{R_{tumor}} \right) \frac{Pe_{L,tumor}}{e^{Pe_{L,tumor}} - 1} \quad (B-11) \\ &+ J_{S,tumor}(1 - \sigma_{S,x})C_{v,tumor} + PS_{S,tumor} \left(C_{v,tumor} - \frac{C_{i,tumor}^f}{R_{tumor}} \right) \frac{Pe_{S,tumor}}{e^{Pe_{S,tumor}} - 1} \\ &- k_{antigen}^{f,sp} C_{i,tumor}^f (B_{max} - C_{i,antigen}^b) V_{i,tumor} + k_{antigen}^{b,sp} C_{i,tumor}^b V_{i,tumor} \\ &- k_{tumor}^f C_{i,tumor}^f V_{i,tumor} + k_{tumor}^b C_{i,tumor}^b V_{i,tumor} - L_{tumor} C_{i,tumor}^f \end{aligned}$$

Interstitial Space – Bound Concentration

The binding of specific antibody is assumed to be saturable and reversible

$$\begin{aligned} V_{i,tumor} \left(\frac{dC_{i,antigen}^b}{dt} \right) &= k_{antigen}^{f,sp} C_{i,tumor}^f (B_{max} - C_{i,antigen}^b) V_{i,tumor} \quad (B-12) \\ &- k_{antigen}^{b,sp} C_{i,antigen}^b V_{i,tumor} - k_{EL,antigen} C_{i,antigen}^b V_{i,tumor} \end{aligned}$$

Here $k_{antigen}^f$ is the forward(association) rate constant, $k_{antigen}^b$ is the reverse-(disassociation) rate constant. B_{max} is the bound concentration at saturation, which is equal to the concentration of tumor associated antigen.

For nonspecific antibody, there is reversible, nonsaturable kinetics with the concentration given by

$$\begin{aligned} V_{i,tumor} \left(\frac{dC_{i,tumor}^b}{dt} \right) &= k_{tumor}^f C_{i,tumor}^f V_{i,tumor} - k_{tumor}^b C_{i,tumor}^b V_{i,tumor} - k_{EL,tumor} C_{i,tumor}^b V_{i,tumor} \quad (B-13) \end{aligned}$$

B.5 Mass Balance Equations for Kidney

For the kidney, the mass balance equations are essentially the same except that the antibody/fragment may be eliminated from the kidney through urine. This is assumed to be a first order process with respect to the vascular concentration with rate constant, U . Note that this is an approximate model of the kidney which does not include a precise description of renal physiology, yet it is adequate to describe whole-body clearance.

Vascular Space

$$\begin{aligned} V_{v,kidney} \left(\frac{dC_{v,kidney}}{dt} \right) &= Q_{kidney} C_{pl} - (Q_{kidney} - L_{kidney})C_{v,liver} - UC_{v,kidney} \quad (B-14) \\ &- J_{L,kidney}(1 - \sigma_{L,x})C_{v,kidney} - PS_{L,kidney} \left(C_{v,kidney} - \frac{C_{i,kidney}^f}{R_{kidney}} \right) \frac{Pe_{L,kidney}}{e^{Pe_{L,kidney}} - 1} \\ &- J_{S,kidney}(1 - \sigma_{S,x})C_{v,kidney} - PS_{S,kidney} \left(C_{v,kidney} - \frac{C_{i,kidney}^f}{R_{kidney}} \right) \frac{Pe_{S,kidney}}{e^{Pe_{S,kidney}} - 1} \end{aligned}$$

Interstitial Space – Free Concentration

$$V_{i,kidney} \left(\frac{dC_{i,kidney}^f}{dt} \right) = J_{L,kidney} (1 - \sigma_{L,x}) C_{v,kidney} + PS_{L,kidney} \left(C_{v,kidney} - \frac{C_{i,kidney}^f}{R_{kidney}} \right) \frac{Pe_{L,kidney}}{e^{Pe_{L,kidney}} - 1} + J_{S,kidney} (1 - \sigma_{S,x}) C_{v,kidney} + PS_{S,kidney} \left(C_{v,kidney} - \frac{C_{i,kidney}^f}{R_{kidney}} \right) \frac{Pe_{S,kidney}}{e^{Pe_{S,kidney}} - 1} - k_{i,kidney}^f C_{i,kidney}^f V_{i,kidney} + k_{i,kidney}^b C_{i,kidney}^b V_{i,kidney} - L_{kidney} C_{i,kidney}^f \quad (B-15)$$

Interstitial Space – Bound Concentration

$$V_{i,kidney} \left(\frac{dC_{i,kidney}^b}{dt} \right) = k_{i,kidney}^f C_{i,kidney}^f V_{i,kidney} - k_{i,kidney}^b C_{i,kidney}^b V_{i,kidney} - k_{EL,kidney} C_{i,kidney}^b V_{i,kidney} \quad (B-16)$$

B.6 Mass Balance Equations for Other Organs

For other vital organs (GI tract, spleen, skin, muscle, bone, and heart), the corresponding mass balance equations are identical in their form.

Vascular Space

$$V_{v,organ} \left(\frac{dC_{v,organ}}{dt} \right) = Q_{organ} C_{pl} - (Q_{organ} - L_{organ}) C_{v,organ} - J_{L,organ} (1 - \sigma_{L,x}) C_{v,organ} - PS_{L,organ} \left(C_{v,organ} - \frac{C_{i,organ}^f}{R_{organ}} \right) \frac{Pe_{L,organ}}{e^{Pe_{L,organ}} - 1} - J_{S,organ} (1 - \sigma_{S,x}) C_{v,organ} - PS_{S,organ} \left(C_{v,organ} - \frac{C_{i,organ}^f}{R_{organ}} \right) \frac{Pe_{S,organ}}{e^{Pe_{S,organ}} - 1} \quad (B-17)$$

Interstitial Space – Free Concentration

$$V_{i,organ} \left(\frac{dC_{i,organ}^f}{dt} \right) = J_{L,organ} (1 - \sigma_{L,x}) C_{v,organ} + PS_{L,organ} \left(C_{v,organ} - \frac{C_{i,organ}^f}{R_{organ}} \right) \frac{Pe_{L,organ}}{e^{Pe_{L,organ}} - 1} + J_{S,organ} (1 - \sigma_{S,x}) C_{v,organ} + PS_{S,organ} \left(C_{v,organ} - \frac{C_{i,organ}^f}{R_{organ}} \right) \frac{Pe_{S,organ}}{e^{Pe_{S,organ}} - 1} - k_{i,organ}^f C_{i,organ}^f V_{i,organ} + k_{i,organ}^b C_{i,organ}^b V_{i,organ} - L_{organ} C_{i,organ}^f \quad (B-18)$$

Interstitial Space – Bound Concentration

$$V_{i,organ} \left(\frac{dC_{i,organ}^b}{dt} \right) = k_{i,organ}^f C_{i,organ}^f V_{i,organ} - k_{i,organ}^b C_{i,organ}^b V_{i,organ} - k_{EL,organ} C_{i,organ}^b V_{i,organ} \quad (B-19)$$

In each organ, the total (or average) concentration (Figs. 1–4) is the weighted average of the concentrations within each subcompartment

$$C_{TOT} = \frac{C_v V_v + (C_i^f + C_i^b) V_i}{V_{TOT}} \quad (B-20)$$

REFERENCES

- Jain, R. K. Delivery of novel therapeutic agents in tumors: physiological barriers and strategies. *J. Natl. Cancer Inst.*, 81: 570–576, 1989.
- Sands, H. Radiolabeled monoclonal antibodies for cancer therapy and diagnosis: is it really a chimera? *J. Nucl. Med.*, 33: 29–32, 1992. Chen, H-S., G., and Gross, J. F. Physiologically based pharmacokinetic models for anticancer drugs. *Cancer Chemother. Pharmacol.*, 2: 85–94, 1979.
- Chen, H-S., G., and Gross, J. F. Physiologically based pharmacokinetic models for anticancer drugs. *Cancer Chemother. Pharmacol.*, 2: 85–94, 1979.
- Gerlowski, L. E., and Jain, R. K. Physiologically based pharmacokinetic modeling:

- principles and applications. *J. Pharm. Sci.*, 72: 1103–1123, 1983.
- Strand, S-E., Zanzonico, P., and Johnson, T. Pharmacokinetic modeling. *Med. Phys.*, 20: 515–527, 1993.
- Covell, D. G., Barbet, J., Holton, O. D., Black, C. D. V., Parker, R. J., and Weinstein, J. N. Pharmacokinetics of monoclonal immunoglobulin G1, F(ab')₂ and Fab' in mice. *Cancer Res.*, 46: 3969–3978, 1986.
- Yuan, F., Baxter, L. T., and Jain, R. K. Pharmacokinetic analysis of two-step approaches using bifunctional and enzyme-conjugated antibodies. *Cancer Res.*, 51: 3119–3130, 1991.
- Baxter, L. T., Yuan, F., and Jain, R. K. Pharmacokinetic analysis of the perivascular distribution of bifunctional antibodies and haptens: comparison with experimental data. *Cancer Res.*, 52: 5838–5844, 1992.
- Rippe, B., and Haraldsson, B. Fluid and protein fluxes across small and large pores in the microvasculature. Application of two-pore equations. *Acta Physiol. Scand.*, 131: 411–428, 1987.
- Halpern, S. E., Hagan, P. L., Garver, P. R., Koziol, J. A., Chen, A. W., Frincke, J. M., Bartholomew, R. M., David, G. S., and Adams, T. H. Stability, characterization and kinetics of 111In-labelled monoclonal antitumor antibodies in normal animals and nude mouse-human tumor models. *Cancer Res.*, 43: 5347–5355, 1983.
- Haskell, C. M., Buchegger, F., Schreyer, M., Carrel, S., and Mach, J-P. Monoclonal antibodies to carcinoembryonic antigen: ionic strength as a factor in the selection of antibodies for immunoscintigraphy. *Cancer Res.*, 43: 3857–3864, 1983.
- Friedman, J. Muscle blood flow and Rb86 extraction: Rb86 as a capillary flow indicator. *Am. J. Physiol.*, 214: 488–493, 1968.
- Kitagawa, H., Ohkouchi, E., Fukuda, A., Imai, K., and Yachi, A. Characterization of carcinoembryonic antigen-specific monoclonal antibodies and specific carcinoembryonic antigen assay in sera of patients. *Jpn. J. Cancer Res.*, 77: 922–930, 1986.
- Nap, M., Hammarström, M-L., Börner, O., Hammarström, S., Wagener, C., Handt, S., Schreyer, M., Mach, J-P, Buchegger, F., von Kleist, S., Grunert, F., Seguin, P., Fuks, A., Holm, R., and Lamerz, R. Specificity and affinity of monoclonal antibodies against carcinoembryonic antigen. *Cancer Res.*, 52: 2329–2339, 1992.
- Bischoff, K. B., Dedrick, R. L., Zaharko, D. S., and Longstreth, J. A. Methotrexate pharmacokinetics. *J. Pharm. Sci.*, 60: 1128–1133, 1971.
- Dedrick, R. L. Animal scale-up. *J. Pharmacokinet. Biopharm.*, 1: 435–461, 1973.
- Jain, R. K., and Baxter, L. T. Mechanisms of heterogeneous distribution of monoclonal antibodies and other macromolecules in tumors: significance of interstitial pressure. *Cancer Res.*, 48: 7022–7032, 1988.
- Boucher, Y., Baxter, L. T., and Jain, R. K. Interstitial pressure gradients in tissue-isolated and subcutaneous tumors: implications for therapy. *Cancer Res.*, 50: 4478–4484, 1990.
- Boucher, Y., and Jain, R. K. Microvascular pressure is the principal driving force for interstitial hypertension in solid tumors: implications for vascular collapse. *Cancer Res.*, 52: 5110–5114, 1992.
- Jain, R. K. Transport of molecules in the tumor interstitium: a review. *Cancer Res.*, 47: 3039–3051, 1987.
- Jain, R. K. Determinants of tumor blood flow: a review. *Cancer Res.*, 48: 2641–2658, 1988.
- Gullino, P. M. Extracellular compartments of solid tumors. In: F. F. Becker (ed.), pp. 327–354. *Cancer*. New York: Plenum Publishing Corp., 1975.
- Nugent, L. J., and Jain, R. K. Extravascular diffusion in normal and neoplastic tissues. *Cancer Res.*, 44: 238–244, 1984.
- Clauss, M. A., and Jain, R. K. Interstitial transport of rabbit and sheep antibodies in normal and neoplastic tissues. *Cancer Res.*, 50: 3487–3492, 1990.
- Gerlowski, L. E., and Jain, R. K. Microvascular permeability of normal and neoplastic tissues. *Microvasc. Res.*, 31: 288–305, 1986.
- Jain, R. K. Transport of molecules across tumor vasculature. *Cancer Metastasis Rev.*, 6: 559–594, 1987.
- Yuan, F., Leunig, M., Berk, D. A., and Jain, R. K. Microvascular permeability of albumin, vascular surface area and vascular volume measured in human adenocarcinoma LS174T using dorsal chamber in SCID mice. *Microvasc. Res.*, 45: 269–289, 1993.
- Baxter, L. T., and Jain, R. K. Transport of fluid and macromolecules in tumors. III. Role of binding and metabolism. *Microvasc. Res.*, 41: 5–23, 1991.
- Martin, K. W., and Halpern, S. E. Carcinoembryonic antigen production, secretion, and kinetics in BALB/c mice and a nude mouse tumor model. *Cancer Res.*, 44: 5475–5481, 1984.
- Kaufman, E. N., and Jain, R. K. *In vitro* measurement and screening of monoclonal antibody affinity using fluorescence photobleaching. *J. Immunol. Methods*, 155: 1–17, 1992.
- Kaufman, E. N., and Jain, R. K. Effect of bivalent interaction upon apparent antibody affinity: experimental confirmation of theory using fluorescence photobleaching and implications for antibody binding assays. *Cancer Res.*, 52: 4157–4167, 1992.
- Sharkey, R., Motta-Hennessy, C., Pawlyk, D., Siegel, J., and Goldenberg, D. Biodistribution and radiation dose estimates for yttrium- and iodine-labeled monoclonal antibody IgG fragments in nude mice bearing human colonic tumor xenografts. *Cancer Res.*, 50: 2330–2336, 1990.
- Baxter, L. T., and Jain, R. K. Vascular permeability and interstitial diffusion in superfused tissues: a two-dimensional model. *Microvasc. Res.*, 36: 108–115, 1988.
- Baxter, L. T., and Jain, R. K. Transport of fluid and macromolecules in tumors. I. Role of interstitial pressure and convection. *Microvasc. Res.*, 37: 77–104, 1989.
- Fujimori, K., Covell, D. G., Fletcher, J. E., and Weinstein, J. N. Modeling analysis of the global and microscopic distribution of Immunoglobulin G, F(ab')₂, and Fab in tumors. *Cancer Res.*, 49: 5656–5663, 1989.
- Baxter, L. T., and Jain, R. K. Transport of fluid and macromolecules in tumors. II. Role of heterogeneous perfusion and lymphatics. *Microvasc. Res.*, 40: 246–263, 1990.

37. Baxter, L. T., and Jain, R. K. Transport of fluid and macromolecules in tumors. IV. A microscopic model of the perivascular distribution. *Microvasc. Res.*, 41: 252-272, 1991.
38. Fujimori, K., Fisher, D. R., and Weinstein, J. N. Integrated microscopic-macroscopic pharmacology of monoclonal antibody radioconjugates: the radiation dose distribution. *Cancer Res.*, 51: 4821-4827, 1991.
39. van Osdol, W., Fujimori, K., and Weinstein, J. N. An analysis of monoclonal antibody distribution in microscopic tumor nodules: consequences of a "binding site barrier." *Cancer Res.*, 51: 4776-4784, 1991.
40. Sung, C., Youle, R. J., and Dedrick, R. L. Pharmacokinetic analysis of immunotoxin uptake in solid tumors: role of plasma kinetics, capillary permeability, and binding. *Cancer Res.*, 50: 7382-7392, 1990.
41. Sung, C., Shockley, T. R., Morrison, P. F., Dvorak, H. F., Yarmush, M. L., and Dedrick, R. L. Predicted and observed effects of antibody affinity and antigen density on monoclonal antibody uptake in solid tumors. *Cancer Res.*, 52: 377-384, 1992.
42. Sevcik, E. M., and Jain, R. K. Measurement of capillary filtration coefficient in a solid tumor. *Cancer Res.*, 51: 1352-1355, 1991.
43. Butler, T. P., Grantham, F. H., and Gullino, P. M. Bulk transfer of fluid in the interstitial compartment of mammary tumors. *Cancer Res.*, 35: 3084-3088, 1975.
44. Aukland, K., and Nicolaysen, G. Interstitial fluid volume: local regulatory mechanisms. *Physiol. Rev.*, 61: 556-643, 1981.
45. Fujimori, K., Covell, D., Fletcher, J., and Weinstein, J. A modeling analysis of monoclonal antibody percolation through tumors: a binding-site barrier. *J. Nucl. Med.*, 31: 1191-1198, 1990.
46. Juweid, M., Neumann, R., Paik, C., Perez-Bacete, J., Sato, J., van Osdol, W., and Weinstein, J. The micropharmacology of monoclonal antibodies in solid tumors: direct experimental evidence for a binding site barrier. *Cancer Res.*, 52: 5144-5153, 1992.
47. Weinstein, J., and van Osdol, W. Early intervention in cancer using monoclonal antibodies and other biological ligands: micropharmacology and the "binding-site barrier." *Cancer Res.*, 52: 2747s-2751s, 1992.
48. Hindmarsh, A. C. LSODE and LSODI, two new initial value ordinary differential equation solvers. *ACM Signum Newsletter*, 15: 10-11, 1980.

Physiologically Based Pharmacokinetic Model for Specific and Nonspecific Monoclonal Antibodies and Fragments in Normal Tissues and Human Tumor Xenografts in Nude Mice

Laurence T. Baxter, Hui Zhu, Daniel G. Mackensen, et al.

Cancer Res 1994;54:1517-1528.

Updated version Access the most recent version of this article at:
<http://cancerres.aacrjournals.org/content/54/6/1517>

E-mail alerts	Sign up to receive free email-alerts related to this article or journal.
Reprints and Subscriptions	To order reprints of this article or to subscribe to the journal, contact the AACR Publications Department at pubs@aacr.org .
Permissions	To request permission to re-use all or part of this article, use this link http://cancerres.aacrjournals.org/content/54/6/1517 . Click on "Request Permissions" which will take you to the Copyright Clearance Center's (CCC) Rightslink site.